Research Article | Vol. 25, No. 21 | 16 Oct 2017 | OPTICS EXPRESS 25079
Optics EXPRESS

Polarisation structuring of broadband light

KEVIN J. MITCHELL,[1,*] NEAL RADWELL,[1] SONJA FRANKE-ARNOLD,[1] MILES J. PADGETT,[1] AND DAVID B. PHILLIPS[1,2]

[1] School of Physics and Astronomy, University of Glasgow, Glasgow G12 8QQ, Scotland, UK
[2] School of Physics, University of Exeter, Stocker Road, Exeter EX4 4QL, UK
[*] k.mitchell.1@research.gla.ac.uk

Abstract: Spatial structuring of the intensity, phase and polarisation of light is useful in a wide variety of modern applications, from microscopy to optical communications. This shaping is most commonly achieved using liquid crystal spatial light modulators (LC-SLMs). However, the inherent chromatic dispersion of LC-SLMs when used as diffractive elements presents a challenge to the extension of such techniques from monochromatic to broadband light. In this work we demonstrate a method of generating broadband vector beams with dynamically tunable intensity, phase and polarisation over a bandwidth of 100 nm. We use our system to generate radially and azimuthally polarised vector vortex beams carrying orbital angular momentum, and beams whose polarisation states span the majority of the Poincaré sphere. We characterise these broadband vector beams using spatially and spectrally resolved Stokes measurements, and detail the technical and fundamental limitations of our technique, including beam generation fidelity and efficiency. The broadband vector beam shaper that we demonstrate here may find use in applications such as ultrafast beam shaping and white light microscopy.

OCIS codes: (050.1970) Diffractive optics; (050.4865) Optical vortices; (260.5430) Polarization; (140.3300) Laser beam shaping; (130.2035) Dispersion compensation devices; (230.6120) Spatial light modulators.

References and links

1. J. Wang, J. Y. Yang, I. M. Fazal, N. Ahmed, Y. Yan, H. Huang, Y. Ren, Y. Yue, S. Dolinar, M. Tur, and A. E. Willner, "Terabit free-space data transmission employing orbital angular momentum multiplexing," Nat. Photonics **6**(7), 488–496 (2012).
2. E. R. Dufresne, G. C. Spalding, M. T. Dearing, S. A. Sheets, and D. G. Grier, "Computer-generated holographic optical tweezer arrays," Rev. Sci. Instrum. **72**(3), 1810–1816 (2001).
3. C. Maurer, A. Jesacher, S. Bernet, and M. Ritsch-Marte, "What spatial light modulators can do for optical microscopy," Laser Photon. Rev. **5**(1), 81–101 (2011).
4. M. P. Lee, G. M. Gibson, R. Bowman, S. Bernet, M. Ritsch-Marte, D. B. Phillips, and M. J. Padgett, "A multi-modal stereo microscope based on a spatial light modulator," Opt. Express **21**(14), 16541–16551 (2013).
5. J. A. Davis, D. M. Cottrell, J. Campos, M. J. Yzuel and I. Moreno, "Encoding amplitude information onto phase-only filters," Appl. Opt. **38**, 5004–5013 (1999).
6. A. B. Stilgoe, A. V. Kashchuk, D. Preece, and H. Rubinsztein-Dunlop, "An interpretation and guide to single-pass beam shaping methods using SLMs and DMDs," J. Opt. **18**(6), 065609 (2016).
7. C. Maurer, A. Jesacher, S. Fürhapter, S. Bernet, and M. Ritsch-Marte, "Tailoring of arbitrary optical vector beams," New J. Phys. **9**(3), 78 (2007).
8. D. Preece, S. Keen, E. Botvinick, R. Bowman, M. Padgett and J. Leach, "Independent polarisation control of multiple optical traps," Opt. Express **16**, 15897–15902 (2008).
9. F. Kenny, D. Lara, O. G. Rodríguez-Herrera, and C. Dainty, "Complete polarization and phase control for focus-shaping in high-NA microscopy," Opt. Express **20**, 14015–14029 (2012).
10. Z. Chen, T. Zeng, B. Qian, and J. Ding, "Complete shaping of optical vector beams," Opt. Express **23**, 17701–17710 (2015).
11. V. G. Niziev, R. S. Chang and A. V. Nesterov, "Generation of inhomogeneously polarised laser beams by use of a Sagnac interferometer," Appl. Opt. **45**(33), 8393–8399 (2006).
12. R. Dorn, S. Quabis, and G. Leuchs, "Sharper focus for a radially polarized light beam," Phys. Rev. Lett. **91**, 233901 (2003).
13. P. Török and P. R. T. Munro, "The use of Gauss-Laguerre vector beams in STED microscopy," Opt. Express **12**(15), 3605–3617 (2004).

#301877 https://doi.org/10.1364/OE.25.025079
Journal © 2017 Received 7 Jul 2017; revised 25 Aug 2017; accepted 7 Sep 2017; published 2 Oct 2017

Optics EXPRESS

14. L. Marrucci, C. Manzo, and D. Paparo, "Optical spin-to-orbital angular momentum conversion in inhomogeneous anisotropic media," Phys. Rev. Lett. **96**, 163905 (2006).
15. K. J. Mitchell, S. Turtaev, M. J. Padgett, T. Čižmár and D. B. Phillips, "High-speed spatial control of the intensity, phase and polarisation of vector beams using a digital micro-mirror device," Opt. Express **24**(25), 29269–29282 (2016).
16. N. Radwell, R. Hawley, J. Götte, and S. Franke-Arnold, "Achromatic vector vortex beams from a glass cone," Nat. Commun. **7**, 10564 (2016).
17. D. N. Naik, N. A. Saad, D. N. Rao and N. K. Viswanathan, "Ultrashort vortex from a Gaussian pulse- An achromatic-interferometric approach," Sci. Rep. **7**, 2395 (2017).
18. R. L. Fork, O. E. Martinez and J. P. Gordon, "Negative dispersion using pairs of prisms," Opt. Lett. **9**, 150–152 (1984).
19. J. Leach and M. J. Padgett, "Observation of chromatic effects near a white-light vortex," New J. Phys. **5**, 154 (2003).
20. J. Liu and J. Wang, "Demonstration of polarization-insensitive spatial light modulation using a single polarization-sensitive spatial light modulator," Sci. Rep. **5**, 9959 (2015).
21. M. A. Cox, C. Rosales-Guzmán, M. P. J. Lavery, D. J. Versfeld, and A. Forbes, "On the resilience of scalar and vector vortex modes in turbulence," Opt. Express **24**, 18105–18113 (2016).
22. T. W. Clark, R. F. Offer, S. Franke-Arnold, A. S. Arnold and N. Radwell, "Comparison of beam generation techniques using a phase only spatial light modulator," Opt. Express **24**, 6249–6264 (2016).
23. R. W. Bowman, G. M. Gibson, A. Linnenberger, D. B. Phillips, J. A. Grieve, D. M. Carberry, S. Serati, M. J. Miles, and M. J. Padgett, "'red tweezers': Fast, customisable hologram generation for optical tweezers," Comput. Phys. Commun. **185**, 268–273 (2014).
24. A. M. Beckley, T. G. Brown, and M. A. Alonso, "Full Poincaré beams," Opt. Express **18**, 10777–10785 (2010).
25. D. Naidoo, F. S. Roux, A. Dudley, I. Litvin, B. Piccirillo, L. Marrucci, and A. Forbes, "Controlled generation of higher-order Poincaré sphere beams from a laser," Nat. Photonics **10**, 327–332 (2016).
26. T. Čižmár, M. Mazilu, and K. Dholakia, "In situ wavefront correction and its application to micromanipulation," Nat. Photonics **4**, 388–394 (2010).
27. C. Akcay, P. Parrein, and J. P. Rolland, "Estimation of longitudinal resolution in optical coherence imaging," Appl. Opt. **41**, 5256–5262 (2002).
28. A. P. Mosk, A. Lagendijk, G. Lerosey, and M. Fink, "Controlling waves in space and time for imaging and focusing in complex media," Nat. Photonics **6**, 283–292 (2012).
29. K. Shi, P. Li, S. Yin, and Z. Liu, "Chromatic confocal microscopy using supercontinuum light," Opt. Express **12**(10), 2096–2101 (2004).
30. S. Diddams and J. Diels, "Dispersion measurements with white-light interferometry," J. Opt. Soc. Am. B **13**, 1120–1129 (1996).
31. T. Brixner, G. Krampert, T. Pfeifer, R. Selle, G. Gerber, M. Wollenhaupt, O. Graefe, C. Horn, D. Liese, and T. Baumert, "Quantum Control by Ultrafast Polarization Shaping," Phys. Rev. Lett. **92**, 208301 (2004).

1. Introduction

Over the last decade, advances in beam shaping technology have significantly improved our ability to manipulate and exploit the fundamental properties of light. This has led to developments in fields ranging from microscopy to optical communications and micro-manipulation [1–4]. Modern beam shaping techniques allow us to arbitrarily structure the intensity and phase of a light beam [5, 6]; more sophisticated schemes can additionally shape the local polarisation state of monochromatic light [7–11]. This ability to structure polarisation has recently gained interest as it provides an additional degree of control over a light beam, enabling the production of fields beyond the scope of those achievable with uniform polarisation. These include fields possessing sub-diffraction limited features [12, 13], and vector vortex beams which carry orbital angular momentum (OAM) and display spin-orbit coupling [14].

In general, polarisation shaping requires independent spatial control of the intensity and phase of two orthogonal polarisation components. This is most commonly accomplished in a reconfigurable manner using liquid crystal spatial light modulators (LC-SLMs), which can spatially control the phase of incident light. For monochromatic light, arbitrary intensity, phase and polarisation shaping has been demonstrated using LC-SLMs as diffractive elements in a two-stage process [7, 15]: firstly, an LC-SLM is used to diffract an incident beam with a uniform linear polarisation into two independent orders, and the polarisation state of one of these orders is then rotated by 90° (stage 1). Secondly, both orders are recombined onto a common axis using a birefringent element, such as a beam displacer (stage 2). By independently shaping the intensity

Optics EXPRESS

and phase of the two diffraction orders in stage 1, the intensity, phase and polarisation of the resultant monochromatic beam can be controlled.

An extension of this technique to enable broadband intensity, phase, and polarisation structuring is attractive as it would enable polarisation control of white light or ultrashort pulses [16, 17]. However, the method described above is inherently narrow-band as it relies on a diffraction grating to separate incident light into two components, meaning incident broadband light would be chromatically dispersed. In addition, LC-SLMs are only capable of controlling the spatial phase of a single linear polarisation state. Therefore, the challenge in extending the bandwidth of these polarisation shaping techniques lies in simultaneously performing chromatic dispersion compensation in a polarisation insensitive manner while combining beams of orthogonal polarisation to propagate along a common axis. [18, 19].

In this work, we demonstrate an optical system which combines polarisation control and dispersion compensation to create beams with arbitrarily specified intensity, phase and polarisation structures over a bandwidth of up to 100 nm. In our optical setup, stage 2 described above is replaced with a second LC-SLM positioned within a Sagnac interferometer to simultaneously recombine the beams and also compensate for the chromatic dispersion [20, 21]. In this way, we harness the dispersion of the second LC-SLM to exactly reverse the dispersive effects introduced by the first. By including suitable polarisation optics within the Sagnac interferometer, we ensure that the second LC-SLM can operate on both polarisation states [20]. We demonstrate the operation of our system by generating broadband radially and azimuthally polarised beams, and broadband Poincaré beams whose polarisation states span the entirety of the Poincaré sphere. We analyse the resulting beams using spatially and spectrally resolved Stokes measurements, and detail the technical and fundamental limitations of our technique, including beam generation fidelity and efficiency.

2. Experimental setup

Figure 1 shows a schematic of our optical setup. In the first stage, the infrared component of a supercontinuum laser source is removed by filtering between 455-600 nm. We then test the operation of our system at various wavelengths which span a range of 100 nm within this window. The beam is collimated and expanded using lenses F1 and F2 to slightly overfill a first LC-SLM, labelled SLM1, at a small angle of incidence ($\sim 5°$). The hologram displayed on SLM1 is designed to separate this incident beam into two beams diffracted at different angles (shown as beams A and B in Fig. 1). This hologram also enables independent spatial control of the local amplitude and phase within each beam.

Lens F3 Fourier transforms the field leaving SLM1, and aperture APT1 blocks any unwanted orders (e.g. in Fig. 1 the undiffracted zero order leaving SLM1 is shown in grey). The polarisation of beam A is then rotated by 90° using a half-wave plate (HWP1). A combination of glass cover slips are placed in the path of beam B to act as an optical delay element (ODE), to compensate for the optical path length difference introduced by HWP1. The path length difference is fine-tuned by adjusting the number of cover slips and the angle of the ODE by up to $\sim 10°$. To minimise any astigmatism, ideally one would align the ODE normal to the incident beam and choose its thickness to exactly correct for the chromatic dispersion. The beams diffracted from SLM1 also suffer from chromatic dispersion: within each diffracted order (i.e. beams A and B), different wavelengths are transmitted across a range of angles, as illustrated in Fig. 1(i).

The second stage in our setup uses a second LC-SLM (SLM2) placed within a displaced Sagnac interferometer, to simultaneously overlap the beams of orthogonal polarisation and to correct for the chromatic dispersion introduced by the fixed grating period on SLM1. The horizontally polarised beam A (shown in red) passes straight through a polarising beamsplitter (PBS), before its polarisation is rotated 90° by HWP2 to become vertically polarised in order to match the modulation axis of SLM2, which is placed in the image plane of SLM1.

Optics EXPRESS

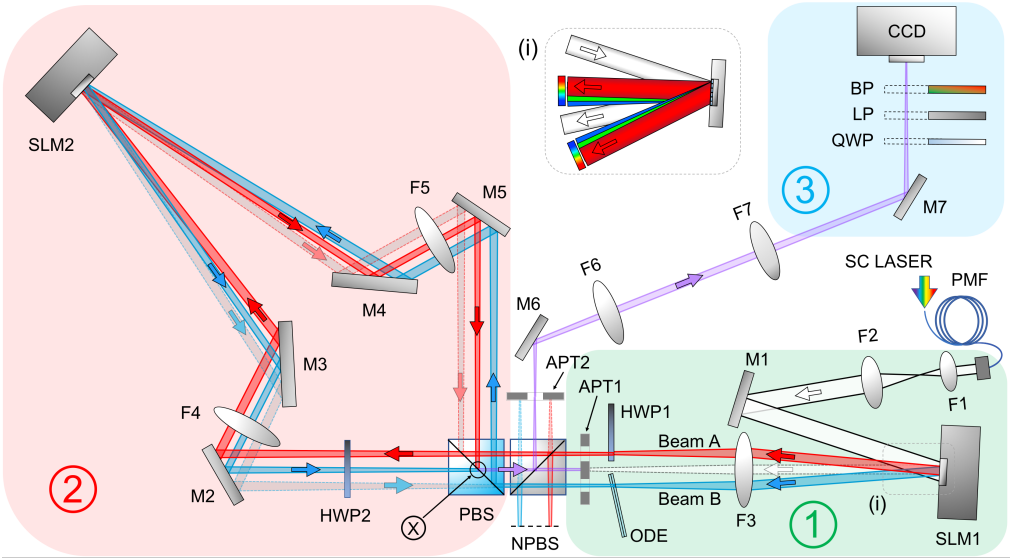

Fig. 1. Experimental setup: Stage 1: beam preparation and shaping. Stage 2: displaced Sagnac interferometer for dispersion compensation and beam combination. Stage 3: vector beam analysis. Main text gives details of operation. SC laser is a Fianium Femtopower 1060 Supercontinuum laser (SC-400-6) filtered to produce an input source of 145 nm bandwidth. PMF is a polarisation-maintaining fibre. Lenses $F1$ and $F2$ have focal lengths of 20 mm and 100 mm respectively, and are used for a 5× beam expansion. SLM1 and SLM2 are both Boulder Nonlinear Systems P512-0635 LC-SLMs. HWP1 and HWP2 are half-wave plates. (N)PBS is a (non-)polarising beamsplitter cube. Lenses $F3 - F5$, of focal length 300 mm, make a 4-F imaging system. M1-M7 are broadband dielectric mirrors. ODE is an optical delay element. LP is a linear polariser. QWP is a quarter-wave plate. BP is an interchangeable bandpass filter. The camera is a Prosilica GC660 CCD. (i) Schematic showing the nature of chromatic dispersion in beams A and B formed by SLM1 in stage 1.

If SLM2 was a mirror, beam A would reflect from it along the upper grey path shown in Fig. 1 and then reflect from the PBS and retrace its path back through the system. Instead we apply a grating to SLM2 which deflects beam A such that it impinges upon the point X within the PBS. This grating applies an angular deviation to beam A that is equal in magnitude but opposite in direction to that applied by SLM1. Thus Beam A is now overlapping and collinear with the optical path of the blocked zero diffraction order from SLM1. This is important because it is only along this optical path that the chromatic dispersion of beams A and B is fully compensated. The vertically polarised beam (Beam B) takes a path in the opposite direction to beam A around the Sagnac interferometer. Beam B already has the correct polarisation for modulation by SLM2, and after deflection by the grating displayed on SLM2, the polarisation of beam B is rotated 90° by HWP2 before it also arrives at point X at the PBS. Therefore beams A and B are both dispersion-compensated, remain orthogonally polarised, and are now overlapping and collinear. The combined beam (shown in purple), exits the PBS via the same port through which beams A and B entered. It is reflected by beamsplitter NPBS before aperture APT2, positioned in the Fourier plane of SLM1 and SLM2, blocks unwanted diffraction orders from SLM2.

The third stage of the set up is used to spatially and spectrally analyse the Stokes parameters of the generated beams. Here the camera is positioned in the Fourier plane of SLMs 1 and 2.

Optics EXPRESS

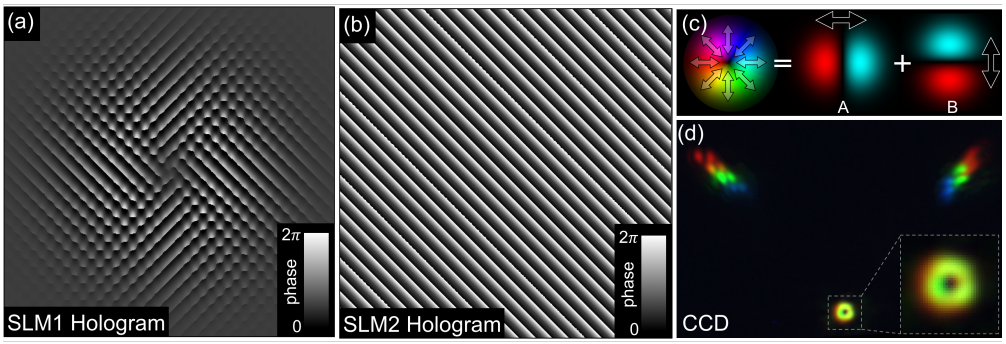

Fig. 2. LC-SLM Hologram design and CCD image of a radially polarised broadband vector vortex beam: (a,b) The holograms displayed on SLM1 (a) and SLM2 (b) to generate a broadband radially polarised beam. (c) A radially polarised vector vortex beam, for example, can be generated by combining a horizontally polarised HG_{10} beam and a vertically polarised HG_{01} beam. (d) A CCD image with aperture APT2 removed and no bandpass filters present in stage 3. All input wavelengths combine to form a broadband vector beam at the lower centre of the panel. As aperture APT2 is removed, the chromatically dispersed zero diffraction orders reflected from SLM2 can also be seen in the upper left and right corners.

3. Hologram design

In this section, we explain how the holograms displayed on SLM1 and SLM2 are designed to create broadband vector beams. The complex forms of beam A and beam B depend upon the required amplitude, phase and polarisation structure of the target beam, as described in detail in [7] and [15]. In short, our aim is to generate an arbitrary broadband vector beam of central wavelength λ_0 in the Fourier plane of SLM1, given by:

$$\vec{E}(x, y, \lambda_0) = \begin{bmatrix} E_{\mathrm{A}}(x, y, \lambda_0) e^{i\phi_{\mathrm{A}}(x,y,\lambda_0)} \\ E_{\mathrm{B}}(x, y, \lambda_0) e^{i\phi_{\mathrm{B}}(x,y,\lambda_0)} \end{bmatrix} \tag{1}$$

where $E_{\mathrm{A,B}}$ is the field amplitude and $\phi_{\mathrm{A,B}}$ the phase of the horizontally and vertically polarised field components respectively, and x, y are Cartesian coordinates across the transverse plane of the target vector beam. With reference to Fig. 1, the spatial modes of beams A and B are therefore given by $\mathbb{E}_{\mathrm{A,B}} = E_{\mathrm{A,B}} e^{i\phi_{\mathrm{A,B}}}$.

The hologram at SLM1 is designed to simultaneously create beams A and B at our central design wavelength λ_0. The complex field required at SLM1 is then given by:

$$\begin{aligned} \mathbb{S}_{\mathrm{dual}}(u, v, \lambda_0) &= W_{\mathrm{rel}} e^{i\phi_{\mathrm{global}}} \mathbb{A} + (1 - W_{\mathrm{rel}}) \mathbb{B} \\ &= S_{\mathrm{dual}}(u, v, \lambda_0) e^{i\phi_{\mathrm{S,dual}}(u,v,\lambda_0)}, \end{aligned} \tag{2}$$

$$\mathbb{A} = \left[\mathfrak{F}(E_{\mathrm{A}} e^{i\phi_{\mathrm{A}}})\right] e^{i(\phi_{\mathrm{A,tilt}})}, \qquad \mathbb{B} = \left[\mathfrak{F}(E_{\mathrm{B}} e^{i\phi_{\mathrm{B}}})\right] e^{i(\phi_{\mathrm{B,tilt}})}, \tag{3}$$

where u and v represent Cartesian co-ordinates across the face of SLM1, and $\mathfrak{F}$ represents the Fourier transform as SLM1 is in the Fourier plane of the target field. Equation (2) includes two parameters, W_{rel} and ϕ_{global} that can be experimentally tuned to optimise the relative power and global phase between beams A and B respectively. W_{rel} is a real number between 0 and 1 which specifies the relative power sent into beams A and B (e.g. the power is nominally the same when W_{rel} is set to 0.5). $\phi_{\mathrm{A,tilt}}$ and $\phi_{\mathrm{B,tilt}}$ are the phase tilts to steer beams A and B to separate positions in the far field of SLM1.

The hologram design requires complex modulation using a phase-only LC-SLM. There are a number of algorithms to achieve this, all of which control the resulting intensity by spatially

Optics EXPRESS

modulating the efficiency of light transmitted into the target diffraction order, and differ only in where they send unwanted light [22, 23]. Here we follow the method described by Davis et al [5]. In short, the amplitude function is encoded as a spatial variation in the contrast of the gratings used to diffract light into the first orders. This variation in contrast spatially modulates the efficiency with which light is diffracted into the first orders, hence allowing us to control the amplitude by introducing spatially varying losses. Assuming the LC-SLM is illuminated with a beam of uniform intensity and phase, the phase hologram to be displayed on SLM1 is given by:

$$H(u, v, \lambda_0) = [1 - \frac{1}{\pi}\text{sinc}^{-1}(S_{\text{dual,norm}}(u, v, \lambda_0))]\phi_{\text{S,dual}}(u, v, \lambda_0) \tag{4}$$

where $S_{\text{dual,norm}}$ is amplitude function S_{dual} normalised to a maximum of 1. Equation 4 therefore represents a hologram which gives complete control of the intensity and phase structure of beams A and B, and also the relative power transmitted into beams A and B.

By choosing appropriate deflection angles of beams A and B from SLM1, the correction at SLM2 can conveniently be achieved with just a single grating. This is possible because upon arrival at SLM2, beam B has undergone an additional mirror flip with respect to beam A (occurring due to its reflection by the PBS). This increases the overall efficiency of the broadband vector beam shaper (see discussion section). The phase tilts given to beams A and B by SLM1, to ensure only a single grating on SLM2 is necessary are:

$$\phi_{\text{A,tilt}}(u, v) = \frac{2\pi}{\lambda_0 f_3}(ux + vy), \qquad \phi_{\text{B,tilt}}(u, v) = \frac{2\pi}{\lambda_0 f_3}(-ux + vy), \tag{5}$$

where λ_0 is the central wavelength of the broadband source. Beam A is located at position (x, y) and beam B at $(-x, y)$ in the Fourier plane of SLM1, where the origin in this frame is the location of the zero order diffracted beam. f_3 is the focal length of lens F3. The above choice of phase tilts means that the single grating displayed on SLM2 is given by:

$$\phi_{\text{SLM2}}(u, v) = \frac{2\pi}{\lambda_0 f_3}(-ux - vy). \tag{6}$$

Figs. 2(a) and 2(b) show examples of the hologram patterns used to generate a broadband radially polarised vector vortex beam.

4. Results

We now demonstrate the generation of broadband vector beams using our system. In stage 3 of the experimental setup (shown in Fig. 1) we characterise the polarisation structure of the generated beams using spatially resolved Stokes measurements, as described in [15, 16]. We perform these Stokes measurements at four different wavelengths over a 100 nm range, using the following bandpass filters: 555.6±4.05 nm, 589±5 nm, 635±3.5 nm and 655.6±6.05 nm. Reference [15] and the captions of Figs. 3-5 provide detail of the fields required on SLM1 to generate the following beams. Figure 3 shows initial system tests to generate linearly and circularly polarised vector beams. Each panel shows an array of polarisation ellipses, describing the ellipticity and orientation of the local polarisation. The local intensity is represented by the semi-major axis of each ellipse and also its brightness. Accompanying insets show a CCD capture of each beam when imaged through the respective bandpass filter.

Figure 4 shows the generation of radially and azimuthally polarised vector vortex beams. We can see that the desired polarisation structure is reproduced in all of the measured wavebands. Because our target beams are generated in the Fourier plane of SLM1, we also observe that the radius of maximum intensity is smaller for shorter wavelengths. Figure 5 shows the generation of Poincaré beams (lemon and star type), whose polarisation spans the majority of the Poincaré sphere [24, 25].

Optics EXPRESS

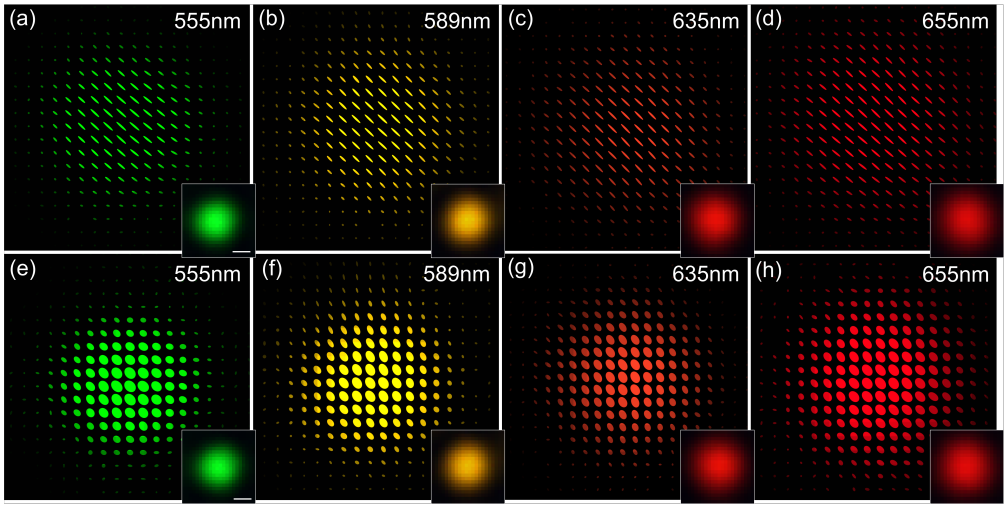

Fig. 3. Experimentally generated broadband vector beams with uniform polarisation: Top row: (a-d) the polarisation ellipse maps of a Gaussian beam whose polarisation is uniformly linear at an angle of 45° shown at the four defined wavebands from 555 nm to 655 nm. In this case the spatial mode of both beams A and B is Gaussian ($HG_{0,0}$), their relative power is equalised, and their global phase difference tuned to 0 radians. All of these parameters are controlled by adjusting the hologram on SLM1. Bottom row: (e-h) when the global phase difference between beam A and B is adjusted to $\pi/2$ radians, we generate a uniformly circularly polarised vector beam. Inset within each polarisation ellipse map is a CCD image showing the intensity with no quarter wave-plate or linear polariser in place in stage 3. Scale bar in (a) and (e) is 30 μm.

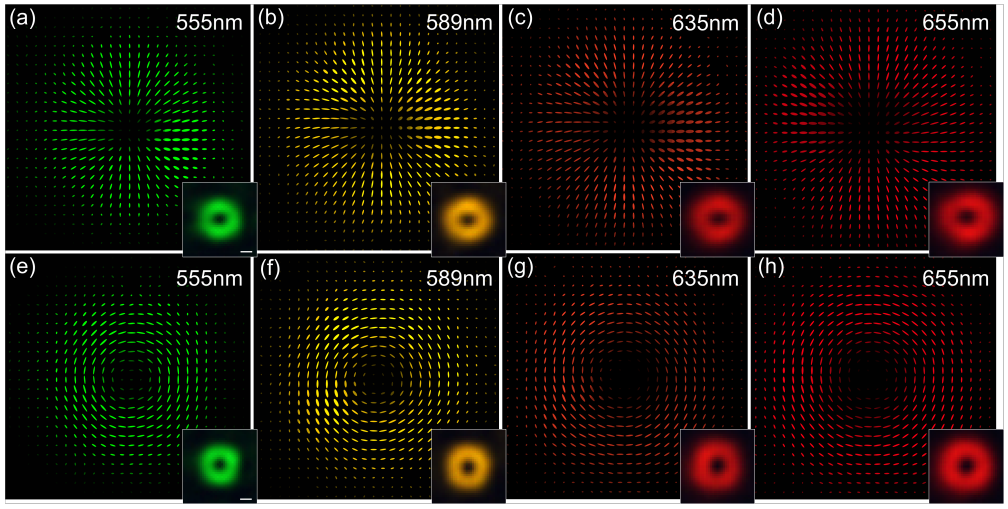

Fig. 4. Experimentally generated broadband vector vortex beams with spatially varying polarisation: Top row: (a-d) in the Fourier plane of SLM2, the experimental broadband polarisation ellipse maps of a broadband radial vector vortex beam. This beam is formed by shaping the spatial mode of beams A and B with an $HG_{1,0}$ and $HG_{0,1}$ mode respectively. Bottom row: an azimuthally polarised vector vortex beam, formed by shaping beams A and B with $HG_{0,1}$ and $HG_{1,0}$ modes respectively. Inset within each polarisation ellipse map is a CCD image detailing the intensity with no quarter wave-plate or linear polariser in place in stage 3. Scale bar in (a) and (e) is 30 μm.

Optics EXPRESS

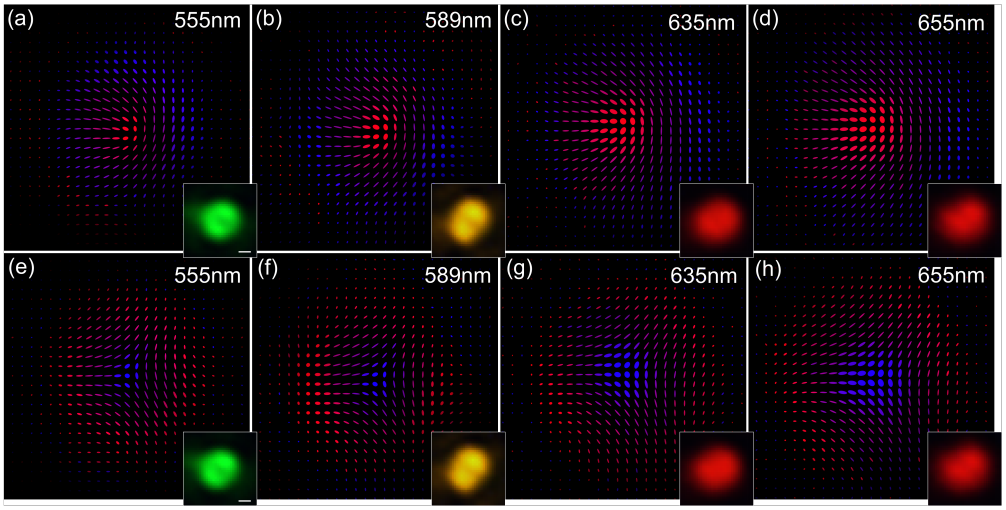

Fig. 5. Experimentally generated broadband Poincaré beams: Top row: (a-d) the "Lemon" Poincaré beam, formed by shaping beam A with modes $LG_{1,0} + LG_{0,0}\exp(i\pi)/2)$ and beam B with modes $LG_{1,0}\exp(i\pi/2) + LG_{0,0}$. Bottom row: (e-h) the "Star" type Poincaré beam, formed by shaping beam A with modes $LG_{1,0}\exp(i\pi/2) + LG_{0,0}$ and beam B with modes $LG_{1,0} + LG_{0,0}\exp(i\pi/2)$. The colour of the ellipses indicates the handedness of the local polarisation state, where blue is left-handed and red is right-handed. Inset within each polarisation ellipse map is a CCD image detailing the intensity with no quarter wave-plate or linear polariser in place in stage 3. Scale bar in (a) and (e) is 30 μm.

5. Discussion and conclusions

There are numerous factors which influence the efficiency, fidelity and bandwidth of our broadband vector beam generator. In general, the beam generation efficiency is below 1 when the desired amplitude of the complex field required at SLM1 does not exactly match the amplitude of the beam incident on SLM1. This effect occurs at all wavelengths, and arises because amplitude shaping using a phase-only LC-SLM is lossy. This efficiency depends strongly on the exact form of the input beam and the desired mode, and is the main theoretical limit to the efficiency of our system [5]. The generation of the radially polarised vector vortex beam of the type shown in Fig. 4 can, for example, be achieved with a theoretical efficiency of $\sim 30\,\%$.

The efficiency of the system is also reduced by the basic optical components, such as the wavelength dependence of half-wave plates and beamsplitters. In addition, in our proof of concept experiment we used a double-pass of a 50:50 non-polarising beamsplitter to out-couple the broadband vector beam, further reducing the efficiency by 75%, following reference [20]. However, in our experiment the displaced Sagnac interferometer configuration spatially separates the input and output beams, and so the NPBS could be replaced with a mirror, thus avoiding this 75% efficiency loss. We note that the efficiency may be further improved by replacing SLM2, which displays a simple phase tilt hologram, with a more efficient static custom-built diffractive optical element.

The hologram on SLM1 is designed for a specific wavelength which can be chosen to be at the centre of the desired operational bandwidth (λ_0). There are several effects that occur when this hologram is illuminated with light of a wavelength other than λ_0. Some of these we can compensate for in our system, but some we cannot. The most evident wavelength dependent effect is angular dispersion which spectrally separates an incident broadband beam. This arises due to the fixed period d of the pattern on the SLM, and can be understood from the grating

Optics EXPRESS

equation defining the diffraction angle, $\theta_m(\lambda)$ of diffraction order m: $\theta_m(\lambda) = \sin^{-1}(m\lambda/d)$. As described above, this form of angular dispersion is compensated for in our system by using SLM2 to generate the opposite angular dispersion to SLM1.

In addition to angular dispersion, the diffraction efficiency and fidelity of our hologram is also wavelength dependent. This is because LC-SLMs operate by controlling the optical path length (OPL) of light travelling through the liquid crystal interface. For a given hologram pixel, the phase change $\delta\phi$ is given by: $\delta\phi = \delta(\mathrm{OPL})/\lambda$, where OPL is the product of the distance travelled through the liquid crystal and its refractive index. Therefore, assuming material dispersion is small, light of wavelength λ will experience a phase pattern that has been rescaled by a factor λ_0/λ. Since amplitude modulation using a phase only LC-SLM is achieved by adjusting the local contrast of the displayed grating, this rescaling means that wavelengths other than λ_0 will experience a grating with a different (and therefore slightly inaccurate) spatially varying contrast. As grating contrast is related to diffracted intensity in a non-linear way (given by Eqn. (4)), then at wavelengths other than λ_0 this effect results in small non-linear departures from the target intensities diffracted into beams A and B.

In order to study the scale of the wavelength dependent effects that we are unable to correct for in our system, we performed a set of simulations. This allowed us to investigate the wavelength dependence of the fidelity and efficiency of our system in the absence of any residual alignment inaccuracies, giving insight into the theoretical limitations of our proposed broadband polarisation shaping method. In our simulation we use scalar diffraction theory to model the propagation of beams of wavelength range $555\,\mathrm{nm} \leq \lambda \leq 655\,\mathrm{nm}$ through our system having diffracted from the hologram on SLM1 that has been designed for wavelength $\lambda_0 = 605\,\mathrm{nm}$. The simulation proceeds as follows: we assume that SLM1 is illuminated by a scalar Gaussian beam $G(u, v, \lambda)$, and the effect of the phase hologram on SLM1 yields a field given by $G.\exp(iH\lambda_0/\lambda)$ at the plane of SLM1. Performing a Fourier transform yields the field at APT1. From this point on beams A and B are orthogonally polarised in our experiment, and so we now separately model the propagation of beams A and B, having passed through each aperture independently. The effect of each aperture is included by multiplying by a binary 2D function that is 1 inside the aperture and 0 elsewhere. A second Fourier transform yields the fields at the plane of SLM2, and the field representing beam B is mirror flipped about the vertical axis to account for the additional mirror reflection in the experiment. The effect of SLM2 is accounted for by multiplying the resulting fields by $\exp.(i\Phi_{\mathrm{SLM2}}\lambda_0/\lambda)$ before a final Fourier transform and the application of APT2. Therefore we have two scalar fields, Ψ_A and Ψ_B, representing the horizontal and vertical field components respectively that arrive at the camera plane. The fidelity F of the generated fields ($0 \leq F \leq 1$) is calculated using:

$$F(\lambda) = \left| \iint \left[\Psi_A^*(x, y, \lambda)\mathbb{E}_{\mathrm{A}}(x, y, \lambda) + \Psi_B^*(x, y, \lambda)\mathbb{E}_{\mathrm{B}}(x, y, \lambda) \right] dxdy \right|^2, \tag{7}$$

where the total intensity of the target field ($|\mathbb{E}_{\mathrm{A}}|^2 + |\mathbb{E}_{\mathrm{B}}|^2$) and the total intensity of the generated fields ($|\Psi_A|^2 + |\Psi_B|^2$) have been normalised to 1. The efficiency of the generated fields can be calculated from the fraction of power lost after each aperture.

Figure 6 shows the simulated performance of our system. Figure 6(a) shows how the fidelity and efficiency of a radially polarised vector beam varies with wavelength. The maximum value of the fidelity is dependent upon choice of aperture sizes and the gradient of the phase tilt diffracting the beams away from the zero diffraction order. Across the entire 100 nm bandwidth the fidelity never falls below 0.995. Insets show a comparison of the intensity of the ideal beam and the generated beam for the lowest fidelity case. The right-hand side shows a comparison of the polarisation structures and individual horizontally and vertically polarised field components in the ideal case and that generated using our proposed method. Interestingly, we observe the efficiency of beam generation increase as the wavelength is reduced. This is because when performing

Optics EXPRESS

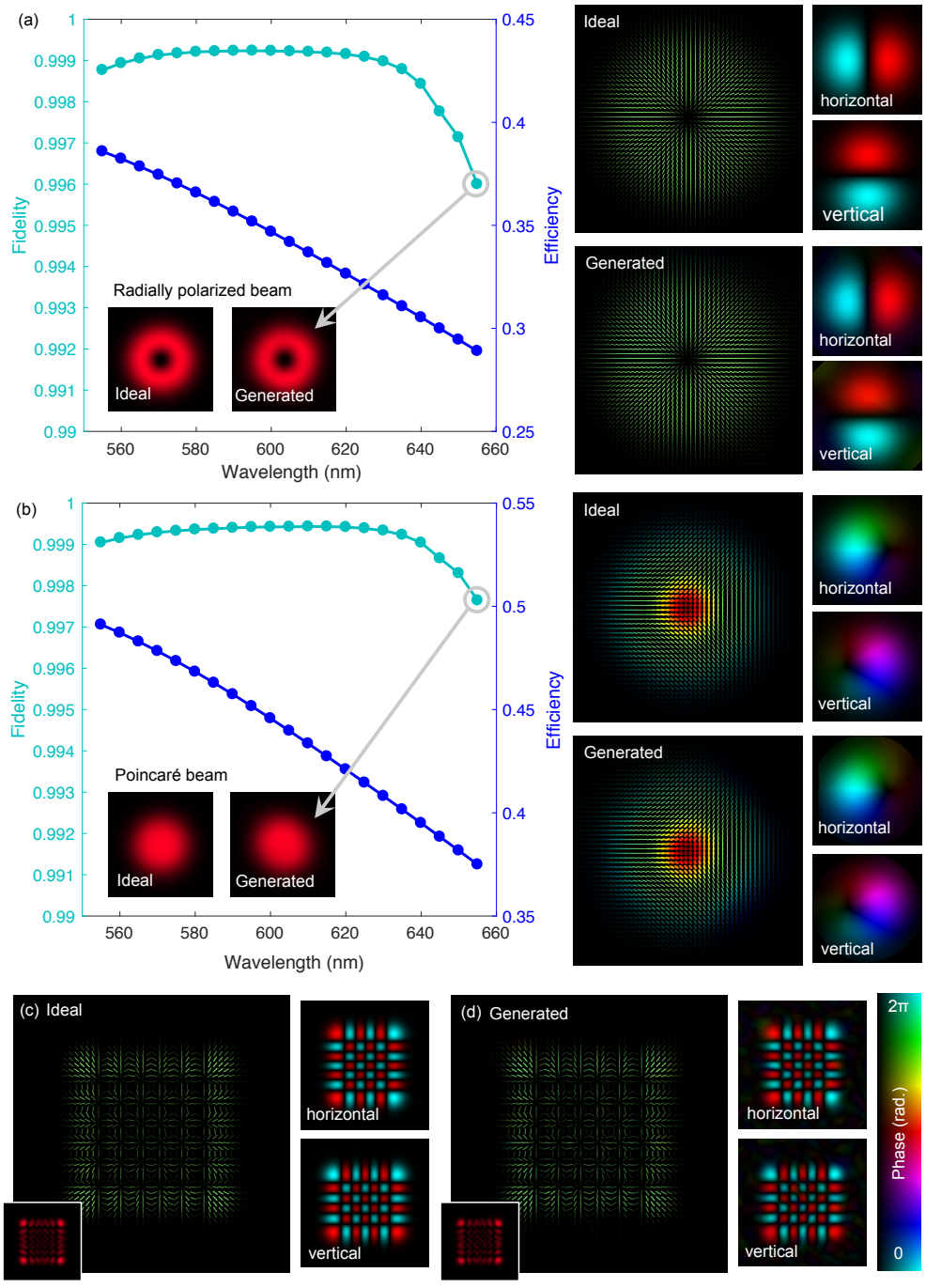

Fig. 6. Simulated performance of our broadband polarisation beam shaper: Fidelity and generation efficiency as a function of wavelength for a radially polarised beam (a), and a "Star" type Poincaré beam (b). Insets within the graphs show ideal and generated beam intensities for the lowest fidelity wavelength (655 nm). Insets to the right-hand side show polarisation maps and beam components in both cases. (c,d) Ideal (c) and generated (d) beams with a more complicated polarisation structure. In this case the illumination wavelength was 655 nm while the SLM1 hologram design wavelength was 605 nm. The construction of this type of beam is considered in more detail in [15].

Optics EXPRESS

phase-only amplitude modulation, it is possible to increase efficiency at the expense of fidelity by thresholding the maximum intensity that S_{dual} is normalised to in Eqn. 4, an effect described in detail in [22] (section: limited beam overlap). When the wavelength is decreased in our system, we believe that an effect analogous to this intensity thresholding occurs, thus increasing the generation efficiency at the expense of a small reduction in fidelity. Figure 6(b) shows that similar trends are seen in the case of the generation of a Poincaré beam. Figures 6(c) and 6(d) show a comparison of the ideal and generated cases in the generation of a beam with a more rapidly varying polarisation structure, which also shows good performance. These effects may contribute towards some of the small polarisation imperfections observed in our experimental results. However, we note that in general these effects appear relatively minor over the bandwidth that we used here.

The experimentally generated polarisation structures are good approximations to the target states for all wavelength bands tested in our set-up. In addition to the minor theoretical effects described above, residual misalignments and aberrations in the optical setup also have a cumulative effect on beam fidelity, and are likely mostly responsible for any reduction in the quality of our experimental results compared to the ideal cases. In general, any undesired intensity and phase variations across beams A and B will modify the ellipticity and orientation of the structured polarisation fields. The LC-SLMs themselves introduce aberrations due to the non-flat nature of their surfaces. For monochromatic beams, in-situ aberration correction can be used to compensate for these defects [26]. However, as above, when using broadband light, such corrective phase masks may only be optimised for a single wavelength (λ_0). The performance of these corrective phase masks will depend on wavelength in a manner analogous to the theoretical effects described in Figs 6(a) and 6(b). We found that applying such phase masks optimised for the central wavelength band did improve the quality of the generated beams across all wavelength bands.

In our proof of concept system, the bandwidth was limited by the spectral response of the wave plates and SLMs (which had anti-reflection coatings optimised for 633 nm) available for the experiment. The stability of the system will also affect the usable bandwidth: in order to generate a coherent polarisation state, the path lengths travelled by beam A and beam B must differ by less than the coherence length defined by the bandwidth of the system. Vibrations that vary the relative path lengths by more than the coherence length will destroy the coherence of the overlapped beams. Therefore, the use of a Sagnac interferometer also offers advantages in stability as vibrations should change both path lengths by the same amount.

In summary, we have demonstrated a technique for generating dynamically reconfigurable broadband vector beams over a bandwidth of 100 nm. This bandwidth corresponds to a coherence time of ~8 fs [27]. Broadband vector beams may find applications in white-light microscopy and ultrafast beam shaping [28–31].

Funding

Royal Academy of Engineering; European Research Council (ERC) (grant 340507); QuantIC Quantum Technology Hub (EP/M01326X/1); Leverhulme Trust (RPG-2013-386).

Acknowledgments

The authors would like to thank Adam Selyem for insightful and useful discussions. We would also like to thank Johannes Courtial for use of his beam modelling software. D.B.P. would like to thank the Royal Academy of Engineering. M.J.P. would like to thank the ERC and the QuantIC Quantum Technology Hub. S.F.A. and N.R. gratefully acknowledge funding by the Leverhulme Trust. The raw data for this article can be found in an open-access repository at http://dx.doi.org/10.5525/gla.researchdata.459.